Carbon 254 (2026) 121428

Contents lists available at ScienceDirect

Carbon

journal homepage: www.elsevier.com/locate/carbon

Polymer-scaffold-guided graphitization for high thermal conductivity in SWCNT-derived carbon fibers

So Jeong Heo [a,b], Jiyeon Kim [a], Jeong-Un Jin [a], Changbeom Jeon [c], Jungwon Kim [a], Nam-Ho You [a], Han Gi Chae [c], Seo Gyun Kim [a,*], Bon-Cheol Ku [a,d,**]

[a] Institute of Advanced Composite Materials, Korea Institute of Science and Technology (KIST), Wanju, 55324, Republic of Korea
[b] Center for Applied Energy Research, University of Kentucky, 2540 Research Park Drive, Lexington, KY, 40511, USA
[c] Department of Materials Science and Engineering, Ulsan National Institute of Science and Technology (UNIST), Ulsan, 44919, Republic of Korea
[d] Department of JBNU-KIST Industry-Academia Convergence Research, Graduate School, Jeonbuk National University, 54896, Republic of Korea

ARTICLE INFO

Keywords:
Carbon nanotube fibers
Polyimide scaffold
Polymer-assisted graphitization
Structural coherence
Thermal conductivity

ABSTRACT

Carbon nanotube (CNT) fibers exhibit outstanding intrinsic properties, yet their macroscopic performance is often limited by structural disorder, void formation, and collapse during high-temperature processing. Here, we introduce a polymer-scaffold-guided graphitization strategy in which polyimide (PI) functions as a thermally stable scaffold to maintain CNT alignment, suppress collapse, and regulate structural evolution. Upon heat treatment up to 2900 °C, the PI-containing CNT fibers exhibited enhanced graphitic ordering, extended axial correlation length, and reduced interlayer spacing, as confirmed by Raman spectroscopy, small-angle and wide-angle X-ray scattering (SAXS and WAXS). Notably, the CNT/PI fiber with 50% PI content achieved a correlation length of 13.7 nm, leading to exceptional thermal conductivity (534 ± 91 W $m^{-1}K^{-1}$), electrical conductivity (0.64 ± 0.02 MS m^{-1}), tensile strength (3.26 ± 0.3 GPa) and modulus (870± 138 GPa). These findings demonstrate that PI acts not only as a reinforcing polymer but also as a structural scaffold that guides graphitization and directional phonon transport, enabling the design of high-performance, anisotropic CNT-based fibers for thermal management and advanced structural applications.

1. Introduction

Carbon nanotubes (CNTs) possess intrinsically high tensile strength (~63 GPa) [1], electrical conductivity (~10^6 S m^{-1}) [2], and thermal conductivity (~6600 W $m^{-1}K^{-1}$) [3], making them promising candidates for advanced functional materials [4–6]. Leveraging their one-dimensional (1D) structure, CNTs have been assembled into macroscopic architectures such as fibers [4,7–9], films [10–12] and foams [13,14] for applications including mechanical, electrical to thermal applications [15–17]. Among these, CNT fibers retain exceptional intrinsic properties of individual nanotubes; however, challenges such as a low aspect ratio and structural imperfections often limit their macroscopic performance [18]. To address these limitations, polymer and carbon materials reinforcement strategies have been introduced [7,19,20]. Polyimide (PI), in particular, is an attractive candidate due to its high mechanical properties [21,22], thermal stability [22,23], and carbon yield upon pyrolysis, rooted in its aromatic backbone [24,25]. In addition, PI can form highly ordered graphitic structures with excellent thermal transport, particularly in films. However, achieving such ordering in fibers is more challenging [24]. As a well-established carbon fiber precursor, PI is an ideal candidate for integrations with CNTs, especially in systems subjected to high-temperature processing. Our efforts [7] to integrate poly(amic acid) (PAA) into CNT dopes in chlorosulfonic acid (CSA) encountered PAA structural instability and leaching into the coagulation bath, hindering high PAA loadings in the composites. In addition, a previous study showed that molecular design plays a key role in promoting phonon transport in PI-based graphitic films, linking structural coherence to enhanced thermal conductivity [26].

A critical but underexplored issue is the anisotropic nature of CNT fiber: phonon scattering and misalignment suppress axial thermal conductivity, highlighting the need to manage structural coherence and directional phonon transport [26]. We hypothesized that PI could function not only as a reinforcing polymer but also as a structural

* Corresponding author.
** Corresponding author. Institute of Advanced Composite Materials, Korea Institute of Science and Technology (KIST), Wanju, 55324, Republic of Korea.
E-mail addresses: seogyun.kim@kist.re.kr (S.G. Kim), cnt@kist.re.kr (B.-C. Ku).

https://doi.org/10.1016/j.carbon.2026.121428
Received 21 October 2025; Received in revised form 4 February 2026; Accepted 19 February 2026
Available online 6 March 2026

scaffold to maintain CNT alignment, suppress collapse, and regulate void evolution under extreme heat treatment. This strategy additionally alleviates the high cost associated with single-walled CNTs, as incorporating up to 50 wt % PI reduces CNT usage and concomitantly improves structural coherence and device material performance.

Here, we demonstrate the fabrication of CNT/PI composite fibers via wet spinning and graphitization up to 2900 °C. Structural analyses via Raman spectroscopy, small-angle and wide-angle X-ray scattering (SAXS and WAXS) reveal that PI effectively stabilizes CNT domains, producing highly graphitic structures with extended correlation length along the fiber axis. This structural control translates into simultaneous optimization of thermal conductivity (534 W $m^{-1}K^{-1}$), electrical conductivity (0.64 MS m^{-1}) and tensile strength (3.26 GPa). Our findings identify PI as a multifunctional scaffold that enables the design of CNT-based fibers with well-defined anisotropic architectures and unprecedented thermal-mechanical performance. Taken together, these results establish a polymer-scaffold-guided graphitization strategy as a viable route to CNT-derived carbon fibers with unprecedented thermal and mechanical performance.

2. Experimental

2.1. Materials and spinning

CNTs which consist of single wall and double wall nanotubes were supplied from Meijo corp. and oxidized at 400 °C for 6 h. To hybridize PI with CNT fiber, polyamic acid (PAA) powder with a 3,3′-diaminobenzidine-co-biphenyltetracarboxylic dianhydride (DAB-BPDA) was thermally imidized to obtain polyimide (PI) powder prior to spinning. The imidization was conducted stepwise at 100 °C, 180 °C, 250 °C, and 350 °C, with a total dwell time of 30 min. CNTs and PI were dissolved in chlorosulfuric acid (CSA) at a concentration of 10 mg mL^{-1}, and the CNT/PI/CSA dope solution-containing up to 60 wt% PI- was extruded through a single nozzle into an acetone coagulation bath at a rate of 0.1 mL min^{-1}. The as-spun fibers were then rinsed continuously in deionized (DI) water and subsequently vacuum-dried at 80 °C for 24 h.

2.2. Heat treatment

The manufactured composite fibers were heat-treated at 1400 °C, 2000 °C, and 2900 °C under a nitrogen and argon atmosphere while applying a constant tensile load of 0.031 N tex^{-1}. A carefully controlled multi-step heating protocol was employed: the temperature was ramped to 1400 °C at 10 °C min^{-1}, to 1700 °C at 5 °C min^{-1}, to 2400 °C at 3 °C min^{-1}, to 2700 °C at 2 °C min^{-1}, and finally to 2900 °C at 1 °C min^{-1}. At each target temperature, the fibers were held isothermally for 30 min to ensure complete transformation.

2.3. Characterization

2.3.1. Properties

Tensile properties were measured using FAVIMAT+ (Textechno) with 1-2 cN at a rate of 2 mm min^{-1}. The linear density of the fibers was determined by analyzing their resonance frequency using a vibroscope of FAVIMAT. To double check, all the fibers were weighted using micro weigh. The specific density of the fibers was measured using a density gradient column (POLYTEST, Ray-Ran, UK), constructed from two immiscible liquids: benzene and 1,1,2,2-tetrabromoethane. Glass beads with certified density values were used to calibrate the column. Fiber samples were immersed in the column and allowed to equilibrate for 24 h. The density results obtained from the gradient method were further verified using the linear density (tex) measured by FAVIMAT+ and cross-sectional areas derived from focused ion beam-scanning electron microscope (FIB-SEM) images (Fig. S1).

The electrical conductivity of the fibers was evaluated using a standard four-point probe method with a probe station (MST-4000A, MS Tech). Thermal conductivity was measured using the self-heating technique, where Joule heating was induced by passing a direct current through the fibers. The resultant temperature increase was monitored through the intrinsic thermoresistive behavior of each fiber using a four-point setup. The measurements were conducted under high vacuum ($\sim 10^{-6}$ Torr), ensuring negligible heat loss via convection and radiation. The total suspended fiber length between the voltage probes was ~4 mm. The temperature rise remained below 10K during the test, with ensured that radiative heat loss remained negligible compared to conductive heat dissipation along the fiber. A summary of the minimum and maximum sample lengths used for thermal conductivity measurements under different heat-treatment temperatures and PI contents is provided in Table S1. Electrical power input was measured with a source meter (Keithley 6221) and the corresponding voltage drop with a nanovoltmeter (Keithley 2182A). Fiber dimensions, including length and cross-sectional area, were measured using optical microscopy and SEM, respectively. The reported values are averages over approximately 20 samples for tensile testing and 10 samples for electrical and thermal conductivity measurements; error bars denote standard deviations.

2.3.2. Structural characterization

The void structure and crystalline characteristics of the fibers were examined using 2D small-angle X-ray scattering (2D-SAXS) and wide-angle X-ray scattering (2D-WAXS). Measurements were performed using a Rigaku MicroMax-007 generator (operated at 45 kV and 66 mA, $\lambda = 0.154$ nm), equipped with a Rigaku R-axis IV++ detector. The sample-to-detector distances (SDD) were set in 3.06 m for SAXS and 0.25 m for WAXS. SAXS data were analyzed to extract correlation lengths in both the meridional and equatorial directions, providing insights into nanoscale structure such as void and correlation length.

Crystallographic analysis of the (002) reflection was carried out from the 2D-WAXS patterns using IGOR pro. The orientation of graphitic domains was quantified via azimuthal intensity scans at $2\theta \approx 26^{\circ}$, and Hermans' orientation factor was calculated using Wilchinsky's equation. The in-plane (La) and out-of-plane (Lc) crystallite sizes were estimated using the Scherrer equation with a shape factor (K) of 0.9.

Cross-sectional morphology of the fibers was further examined using focused ion beam (FIB) milling in an FEI Helios SEM, followed by high-resolution transmission electron microscopy (HR-TEM, FEI Titan Cubed 60-300). Surface chemical composition and bonding states were analyzed by X-ray photoelectron spectroscopy (XPS, Thermo Scientific K-Alpha) using monochromatic Al Kα radiation (1486.6 eV). The functional groups present in PAA and PI were characterized using Fourier-transform infrared spectroscopy (FT-IR, Nicolet IS10) in attenuated total reflectance (ATR) mode, with 256 scans and 4 cm^{-1} resolution.

Raman spectroscopy (InVia Reflex, Renishaw) with a 532 nm excitation laser was used to evaluate the graphitic structure of the fibers. The intensity ratio of D-band to G-band (I_D/I_G) was used to assess the degree of defect, while the 2D-to-G-band ratio (I_{2D}/I_G) provided insight into the extent of graphitic stacking and crystallinity. Liquid crystalline behavior of the CNT/CSA solution was observed via polarized optical microscopy (POM, L150, Nikon) using crossed polarizer.

3. Results and discussion

3.1. Properties of the fibers

Polyimide exhibits exceptional tensile and thermal properties as reported prior researches [7,21–25] and it has a variety of monomer structures. Among the polyimides structures, DHB-BPDA and DAB-BPDA films presented higher thermal conductivity than ODA-PMDA film because their benzene rings in backbone helped to make carbon structure more stable during the carbonization and graphitization with high temperature [27]. However, DHB-BPDA was the most easily to be sulfonated by CSA because of their hydroxyl groups [28], modified bulky

sulfonation groups on backbone of DHB-BPDA hinder the molecular orientation along the fiber axis and tensile properties of the CNT/DAB-BPDA fiber were improved (Fig. S2). Furthermore, PAA is vulnerable to strong acid like CSA [7], therefore, we imidized the PAA powder to obtain PI powder (Fig. S3), which was subsequently confirmed to dissolve in CSA (Fig. S3) and mixed with CNT/CSA solution and PI was hybridized up to 60% for keeping the liquid crystal state of the dope. To systematically investigate the effect of PI content, the total solid concentration of the spinning dope was kept constant with 10 mg mL^{-1} while varying the CNT-to-PI ratio. Stable wet spinning was achieved up to a PI content of 60 wt%. At higher PI contents (≥70 wt%), however, the dope failed to form continuous CNT-based fibers under identical spinning conditions, indicating a transition from a CNT-supported network to a PI-rich matrix. Therefore, compositions above 60 wt% PI were excluded to ensure meaningful structural and property comparisons within a CNT-framework-dominated regime. Hereafter, the CNT composite fibers containing 10%, 30%, 50%, and 60% polyimide are referred to as PI_{10}, PI_{30}, PI_{50}, and PI_{60}, respectively. As-spun fiber was heat treated at 2900 °C to make graphitic structures, and comprehensive properties were evaluated (Fig. 1).

The CNT composite fibers exhibited distinct trends in tensile strength (Fig. 1b) and modulus (Fig. 1a) depending on the PI content. The tensile strength increased with increasing PI content, reaching a maximum of 3.26 ± 0.3 GPa at 50 wt% PI (PI_{50}) (Fig. 1b), while the pristine CNT fibers showed the lowest strength of 1.57 ± 0.2 GPa even after graphitization of the fiber. In contrast, the tensile modulus generally decreased with increasing PI content [7], however, the PI_{50} fiber exhibited a notable recovery in modulus (870 ± 138 GPa), comparable to that of the pristine CNT fiber (811 ± 69 GPa) (Fig. 1a). This divergence between strength and modulus suggests that different structural mechanisms—such as CNT alignment, void structure, and interfacial load transfer—may govern each property. Interestingly, thermal and electrical conductivities followed trends similar to the tensile strength not tensile modulus, both peaking at PI_{50} (Fig. 1c and d). Although the final heat-treatment temperature of commercial carbon fibers is not always disclosed, high-strength grades are generally carbonized, whereas high-modulus grades are typically graphitized at higher temperatures. The graphitized CNT/PI composite fibers exhibited superior thermal conductivity relative to conventional PAN- and pitch-based carbon fibers [29] (Fig. 1e), specifically PAN-based Toray's T-series and M-series, and pitch-based Mitsubishi's K13C and K13D series, along with reduced density (Fig. 1f) for enhanced lightweight performance. Notably, its properties were comparable to, or even exceed, those of M60J fiber (Toray, tensile strength: 3.8 GPa; modulus: 588 GPa; density: 1.93 g cm^{-3}) [30] as well as K13C6U fiber (Mitsubishi, tensile strength: 3.6 GPa; modulus: 900 GPa; density: 2.18 g cm^{-3}) [29] (Fig. 1g). Importantly, our CNT/PI composite fibers achieved a similar balance of high conductivity and relatively low density to K13C6U, highlighting their potential as next-generation high-performance carbon fibers. This simultaneous enhancement in mechanical and transport properties at an optimal PI content at 50% indicated that the structural evolution during processing plays a significant role. It is also noteworthy that the precursor composite fibers, prior to heat treatment, exhibited both lower tensile strength and modulus than the pristine CNT fibers (Fig. S4). This is because, prior to heat treatment, the spaces between CNTs are filled with polymer; however, after heat treatment, these regions are converted into a carbon structure, leading to a shift in the property trend such that the fibers surpass the performance of pristine CNT fibers. However, upon high-temperature graphitization, the composite fibers—particularly PI_{50}—surpassed the CNT-only fibers in both properties. This transition highlights the crucial role of the PI matrix with optimal composition in guiding structural reorganization and densification during thermal treatment, contributing to the final enhancement in performance.

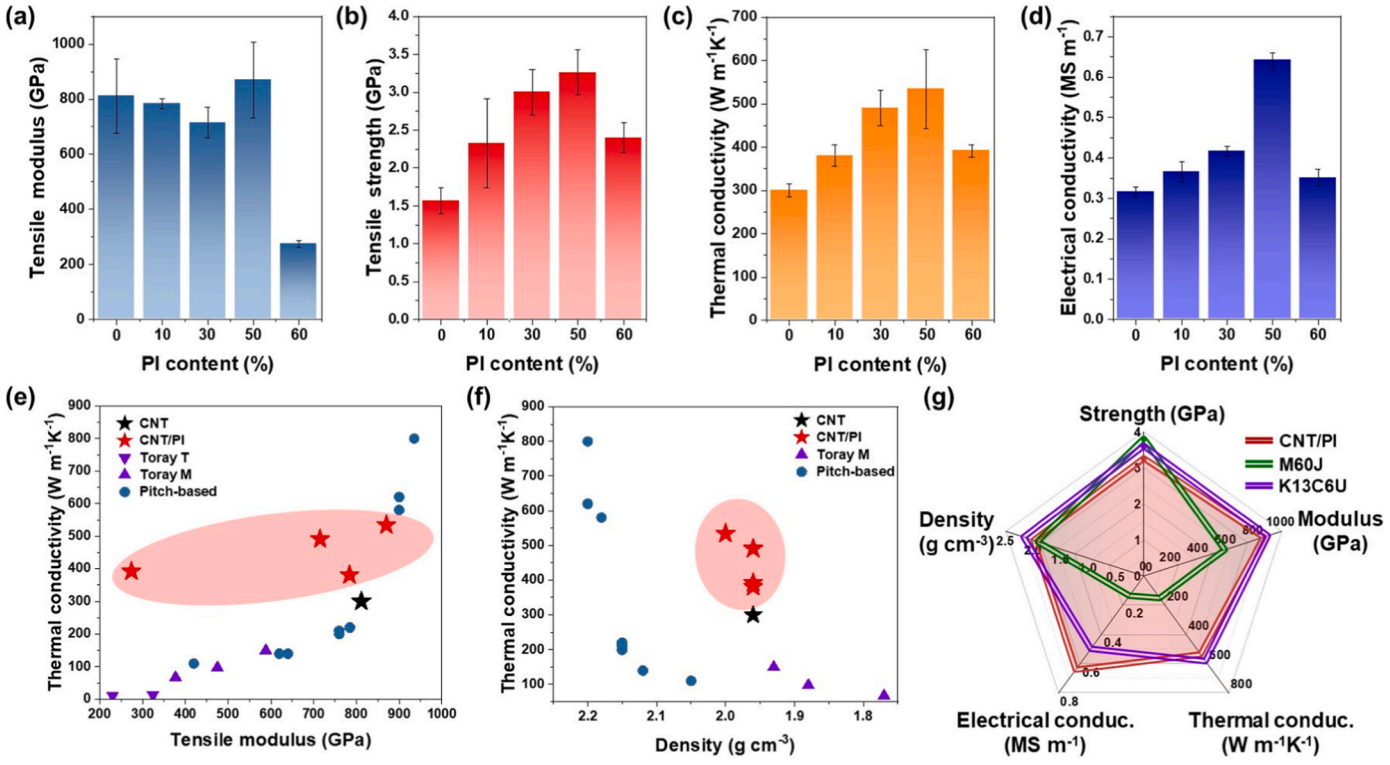

Fig. 1. Overall properties of the fiber graphitized at 2900 °C with PI content from 0 to 60%. (a) Tensile modulus, (b) tensile strength, (c) thermal conductivity and (d) electrical conductivity. Correlated with thermal conductivity with (e) tensile modulus and (f) density of the fiber. (g) Normalized performance profile of CNT/PI composite Fibers with M60J and K13C6U reference.

3.2. Well-ordered nanostructure in PI_{50} fibers evidenced by equatorial SAXS

To elucidate the structural origins of this enhancement, we carried out a series of detailed structural analyses. Typically, fibers which exhibit higher thermal conductivity have larger size of well-oriented crystal plane and crystallinity along the fibers [31,32], however, at extremely high temperature such as 2900 °C with similar materials, it would be similar size of crystal plane regardless of fiber property (Fig. S5). Furthermore, among the fibers, PI_{50} fiber exhibited an exceptional thermal conductivity of 534 ± 91 W m^{-1} K^{-1}, representing an 80% increase relative to pristine CNT fibers. The enhanced properties were attributed to the more ordered structural arrangement or void structure induced by PI incorporation rather than crystal size.

Normally, thermal conductivity of the fiber is very affected by not only the crystal size (La) along the fiber axis but also perpendicular (Lc) to fiber axis [33,34], and we considered both axis of the fiber for properties evaluation and structure characterization. For improvement of the thermal conductivity, prevention of the phonon scattering as well as effective phonon transfer matters regularly arranged structure. Through the SAXS analysis, we obtained 2D SAXS patterns (Fig. 2a) and calculated void structure first by using Ruland and classical porod's method [35,36]. Void misalignment along the fiber axis decreased and void thickness decreased until PI content with 50% increased above the content. Voids within the fiber were typically cylindrical in shape, and their misalignment contributed to increased void thickness. The graphitized PI phase effectively filled the interstitial spaces between CNTs up to a PI content of 50%, thereby reducing both void size and misalignment (Fig. 2b and c). However, beyond this optimal content, the emergence of a PI-rich bulk phase resulted in larger voids, likely due to phase separation or structural heterogeneity at elevated PI concentrations, consistent with previous findings [7]. High-temperature treatment of pristine CNT fibers typically promotes the development of large graphitic domain, which can lead to structural tilting and folding due to anisotropic growth [37]. In contrast, increasing PI content within the CNT/PI composite fibers facilitated a progressive reduction in void misalignment and void thickness, indicating that PI plays a stabilizing role during graphitization. Nevertheless, at PI contents exceeding 50%, the PI-derived bulk phase appeared to disrupt the ordered assembly, compromising structural integrity and mechanical performance [7]. This structural trend in void misalignment was closely associated with the structural regularity of the fibers, as reflected in the intensity distribution in a double logarithmic plot (Fig. 2d), indicating the periodicity and degree of structural organization. To further quantify this regularity, equatorial SAXS profiles were analyzed with a focus on their decay characteristics, as established in prior studies [38,39]. When the internal structure was well-ordered, the scattering intensity ($I(q)$) followed a power-law decay with a nearly constant slope (n) with q-vector

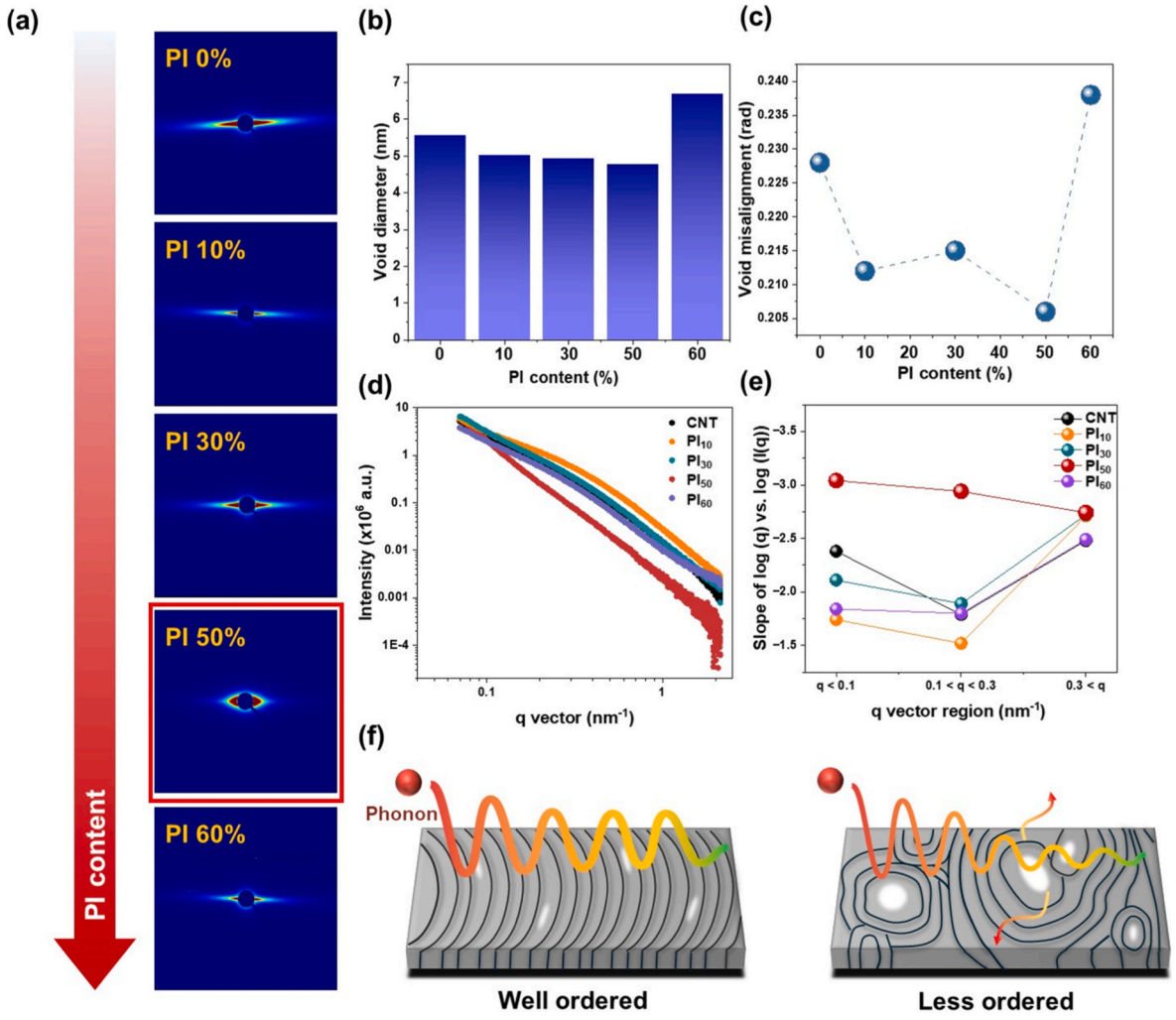

Fig. 2. SAXS analysis of the CNT/PI fibers according to the PI content. (a) 2D SAXS pattern, (b) void diameter, (c) void misalignment, (d) equatorial scans the CNT/PI fibers as PI content, and (e) slope difference in double logarithm plot according to the q region. (f) Scheme of the phonon scattering with structure perpendicular to the fiber axis according to the structural periodicity.

(q), appearing as a straight line on a double logarithmic plot ($I(q) \approx q^{-n}$) [40]. In contrast, decreased structural regularity led to heterogeneous domains, producing slope variation (m) across the q-range and manifesting as Lorentzian-type decay behavior with short correlation length (ξ, $I(q) \approx \frac{1}{(1+(q\xi)^2)^m}$) [41,42]. As shown in SAXS profiles, the graphitized pristine CNT and PI_{10} fibers exhibited a Lorentzian-type decay characterized by a broad and curved profile, which is typically associated with crumpled morphologies or pseudo-phase separation, indicating the most disordered structures among the samples. Notably, the incorporation of PI at 10% did not enhance structural regularity and instead appeared to introduce further heterogeneity (Fig. 2d). With increasing PI content, particularly at 50%, the scattering profile transitioned into a distinct power-law decay with a constant slope, indicative of improved structural ordering like pitch fiber (Fig. S6). At 60% PI content, however, the decay behavior reverted toward a Lorentzian-decay again, suggesting a breakdown of long-range order likely due to phase separation or excessive PI bulk phase interference. Cross-sectional SEM observations (Fig. S1.) provide qualitative support for this interpretation, revealing the presence of irregularly distributed pores within the PI_{60} fibers. Although these pores were not highly abundant, they were distributed nonuniformly across the cross-section, in contrast to the more homogeneous structure observed for PI_{50} fibers, indicating locally disrupted packing and reduced structural coherence. This trend is consistent with the SAXS analysis, which reveals reduced cross-sectional ordering associated with void misalignment and growth. Importantly, despite the larger structural length scales probed by SEM, these morphological irregularities align well with the SAXS signature of increased disorder, reinforcing the conclusion that a PI content of ~50% represents an optimal balance for effective scaffold formation. This trend was also evident in the 2D SAXS patterns (Fig. 2a), where fibers with more regular structure displayed higher intensity and shorter streaks oriented perpendicular to the fiber axis, consistent with enhanced alignment and periodicity. The Lorentzian-decay exhibited distinct slope variations across different q-ranges -low (q were $< 0.1\ nm^{-1}$), mid ($0.1\ nm^{-1} < q < 0.3\ nm^{-1}$) and high ($0.3\ nm^{-1} < q$)-reflecting a distribution of heterogeneous domains. As shown in Fig. 2e, the pristine CNT and the PI_{10}, PI_{30} and PI_{60} fibers all exhibited noticeable slope variations, due to lower structural regularity. In contrast, the CNT/PI_{50} fibers exhibited consistent slopes across all q-ranges (Fig. 2e) like pitch fiber which presents high thermal conductivity, demonstrating highly uniform structural arrangement perpendicular to the fiber axis (Fig. S6). Among the fibers, the PI_{10} showed the most significant slope variation (from −1.52 to −2.71, corresponding to a 78% change), further supporting its disordered nature. In comparison, the graphitized PI_{50} fiber exhibited the most regular alignment, which likely suppressed phonon scattering and enhanced axial thermal transport (Fig. 2f).

3.3. Longest axial periodicity achieved in PI_{50} fibers

While reduced phonon scattering (or dissipation) is essential for improving efficiency of thermal conductivity, facilitating directional phonon transport along the fiber axis is equally critical. To assess this axial transport behavior in relation to structural anisotropy, we analyzed the meridional SAXS profiles using Porod and Debye-Bueche approach [43,44]. Whereas the equatorial decay behavior qualitatively reflects the degree of lateral structural regularity, the meridional analysis allowed us to quantitatively extract the axial correlation length using the Porod-Lorentzain model. These two approaches are complementary, offering both qualitative and quantitative insight into the hierarchical structure of the fibers. The scattering profiles displayed features characteristic of both Porod and Lorentzian (or Cauchy) regimes and were fitted using a combined Porod-Lorentzian model [40]. In this formulation, the correlation length (ξ) reflects the spatial extent of electron density fluctuations within the CNT/PI composite fibers. The model incorporates a high-q Porod term and a low-q Lorentzian term, as shown in the following equation:

$$I(q) = \frac{A}{q^n} + \frac{C}{1+(q\xi)^m} + background$$

Where A and C are the scaling coefficients for Porod and Lorentzian scaling, respectively, and n and m are the corresponding exponents. While the original "correlation length" model was developed for polymer-solvent systems [41,42], it has been applied to heterogeneous solid-state materials with void, including carbon-based systems, to describe structural coherence and electron density fluctuations [43,44]. In this study, we adapted the model in the meridional direction, where the contrast arises from nanoscale voids, graphitic domains, and carbonized PI structures (Fig. 3b and Fig. S7). Notably, correlation length analysis was not conducted using equatorial scans, as reliable fitting could only be achieved for the PI_{50} fiber. In most other fibers, the equatorial SAXS profiles exhibited more pronounced Lorentzian-type decay, suggesting reduced structural regularity and greater disorder perpendicular to the fiber axis. This made it difficult to extract meaningful values ξ in that direction.

Structural regularity of the fibers was assessed through the density fluctuations reflected in $I(q)$, which reflect the spatial distribution of aligned voids and graphitic domain (Fig. 3a and c). A longer correlation length indicates that these features are more uniformly spaced and coherent, corresponding to a more ordered internal structure with fewer phonon-scattering sites. In contrast, shorter correlation lengths signify a disordered arrangement of voids and domains, which disrupts periodicity and hinders phonon transport. Thus, the correlation length provides a quantitative descriptor of the nanoscale structural order, which is directly linked to the thermal and transport properties of the fibers. Among all the fibers, the PI_{50} fiber showed the highest correlation length of 13.7 nm, compared to 3.29 nm for the pristine CNT fiber. This finding highlights the critical role of optimal PI incorporation in promoting structural coherence and improving transport properties along the fiber axis.

Notably, thermal and electrical conductivities showed distinct trends with correlation length. As shown in Fig. 3d, thermal conductivity increased nearly linearly with correlation length, reflecting the sensitivity of phonon transport to nanoscale structural alignment. In contrast, electrical conductivity (Fig. 3e) exhibited a nonlinear, saturating dependence. Unlike phonon transport, electron transport in CNT-based fibers is dominated by inter-tube and inter-domain hoping processes rather than intrinsic band conduction. In this context, the correlation length represents the effective axial extent of continuously aligned sp^2 graphitic domains. A shorter correlation length increases the frequency of inter-crystallite and inter-tube hopping events, leading to higher cumulative contact resistance. As correlation length increases, the number of hopping junctions along the transport pathway is reduced, enabling more efficient carrier transport through extended graphitic domains. Once a critical level of structural coherence is reached, however, further increases in correlation length provide diminishing benefits, as electorn transport remains ultimately limited by residual inter-tube junctions and network connectivity. This mechanism accounts for the observed saturation behavior in electrical conductivity despite continued structural ordering.

3.4. Temperature-dependent structural evolution of pristine CNT vs PI_{50} fibers

Given that the CNT/PI_{50} fiber exhibited the highest correlation length and transport performance, we further investigated its structural evolution across heat-treatment temperatures (1400, 2000, and 2900 °C), in comparison with pristine CNT fibers (Fig. 4). To investigate the structural basis for enhanced performance observed in the PI_{50} fiber, Raman spectroscopy and X-ray scattering analyses were conducted, which revealed temperature-dependent graphitization behavior and

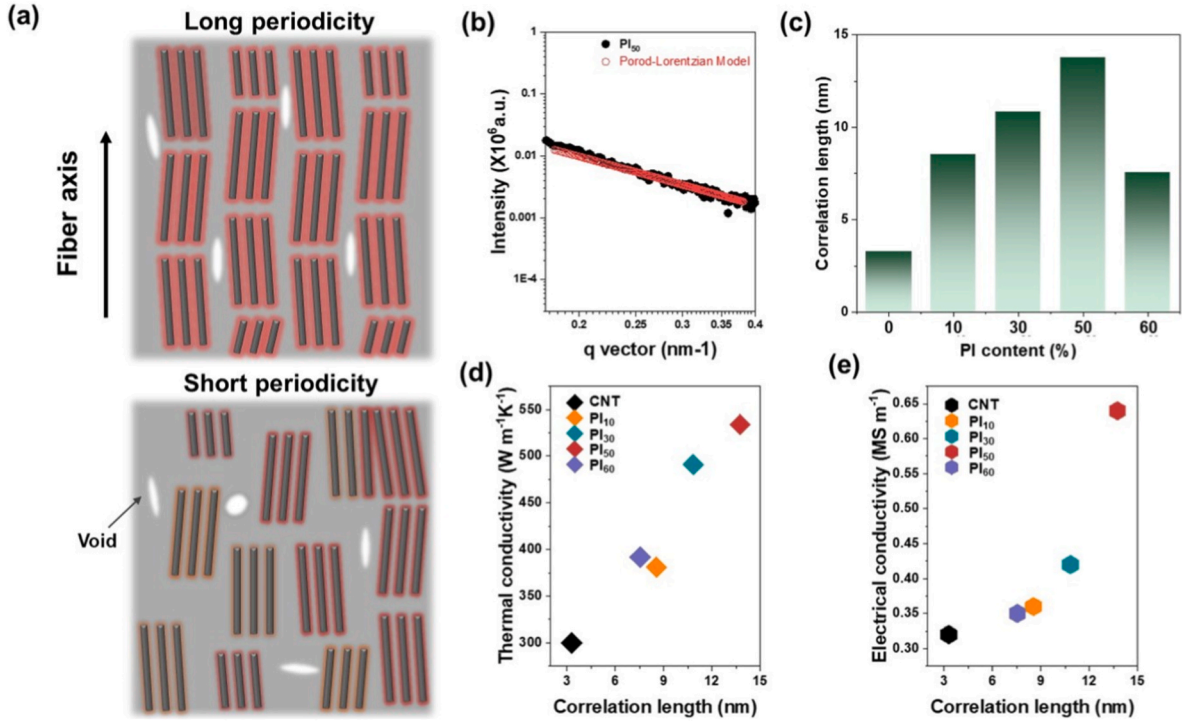

Fig. 3. Correlation length investigation along the fiber axis characterized by SAXS analysis. (a) Scheme of the CNT/PI fibers with meridional direction as structural periodicity, (b) fitted model plot with Porod-Lorentzian model, correlation length of the fiber and relationship with (c) thermal conductivity and (d) electrical conductivity of the fibers.

provided insight into the distinct structural dynamics enabled by PI incorporation. In addition, TEM was employed to directly visualize the graphitic stacking within the fibers, offering complementary evidence of the structural coherence developed through high-temperature treatment (Fig. 4a). As the heat-treatment temperature increased, the G-band of both pristine CNT and CNT/PI fibers exhibited a gradual downshift, indicating stress relaxation and enhanced graphitic ordering within the sp^2 carbon network (Fig. S8). Moreover, the temperature-dependent shifts and intensity changes of the G- and 2D-bands serve as reliable indicators of structural evolution during graphitization. In the fibers, the G-band initially displayed a characteristic splitting into G^- and G^+ components, corresponding to the axial and circumferential vibrations of the CNT lattice [45,46]. This feature was maintained up to 1400 °C, suggesting the persistence of the tubular structure. However, beyond this temperature, the two components gradually merged into a single peak (Fig. S8), signifying the collapse of the tubular form and the transition toward a more planar, graphitic configuration [47]. In parallel, the 2D-band initially downshifted up to 1400 °C, suggesting increasing interlayer interactions and evolving turbostratic stacking (Fig. 4c–f) [48]. In the case of PI_{50} fibers, the 2D-band exhibited a slight upshift at 2000 °C and a more pronounced upshift at 2900 °C, whereas in pristine CNT fibers, the 2D-band downshifted until 2000 °C and only upshifted at 2900 °C as shown in Fig. 4d. This behavior indicates an earlier onset of graphitic ordering in the PI_{50} fibers.

Building on this observation, the marked 2D-band upshift beyond 2000 °C further supports the hypothesis that the PI component began to act as a structural scaffold. In parallel, full width at half maximum (FWHM) decreased continuously up to 2900 °C as shown in Fig. 4e. As the PI was carbonized, it likely reinforced the surrounding CNT framework, mitigating structural collapse and enabling the formation of aligned, well-stacked domains. This interpretation is corroborated by the linear relationship between the I_D/I_G and I_{2D}/I_G ratios (Fig. 4f). Importantly, the temperature-dependent evolution of these Raman metrics for PI_{50} closely follows that of pristine CNT fibers rather than that of pristine PI, whose I_D/I_G and I_{2D}/I_G ratios display markedly different trends (Fig. S9). This divergence indicates that the fundamentally different thermal evolution pathways of the two constituents: PI is carbonized via heteroatom elimination from the polymer backbone and subsequent aromatic domain growth, whereas CNTs retain their tubular framework to high temperatures and reorganize through tube collapse and inter-tube coalescence at elevated temperatures. Accordingly, the divergence indicates that the structure evolution in PI_{50} is not dominated by intrinsic PI graphitization but is instead governed by a scaffold-assisted and reorganization of the CNT network. Although pristine CNT fibers showed higher absolute I_{2D}/I_G values, their concurrently large I_D/I_G ratios indicate the coexistence of localized graphitic domains with significant structural disorder. Notably, both pristine CNT and CNT/PI_{50} fibers exhibited an unusual increase in I_D/I_G ratio with increasing annealing temperature, contrary to the commonly observed trend of defect reduction during graphitization. This anomaly may arise from thermally induced tube collapse or inter-tubes coalescence at extreme temperatures, which can introduce new structural irregularities even as overall graphitic ordering proceeds (Fig. 4f). In contrast, the PI_{50} fibers showed a steeper slope in the I_D/I_G versus I_{2D}/I_G plot, suggesting a more coherent and synchronized evolution toward graphitic ordering. This behavior implies that in PI_{50} fibers, the reduction of defects and the formation of ordered domains progressed in a more structurally coordinated manner, likely enabled by the carbonized PI acting as a physical scaffold. Such structural alignment is essential for optimizing phonon and charge transport, thereby contributing to the superior thermal and electrical performance observed in these fibers. This interpretation is further supported by cross-sectional TEM images of the PI_{50} fibers as shown in Fig. 4a, which reveal pronounced morphological changes with increasing temperature: prior to heat treatment, PI was intercalated between CNT bundles, leading to larger interlayer distances, while selective PI carbonization at 1400 °C initiated scaffold-like filling of voids and improved interfacial contact between CNTs.

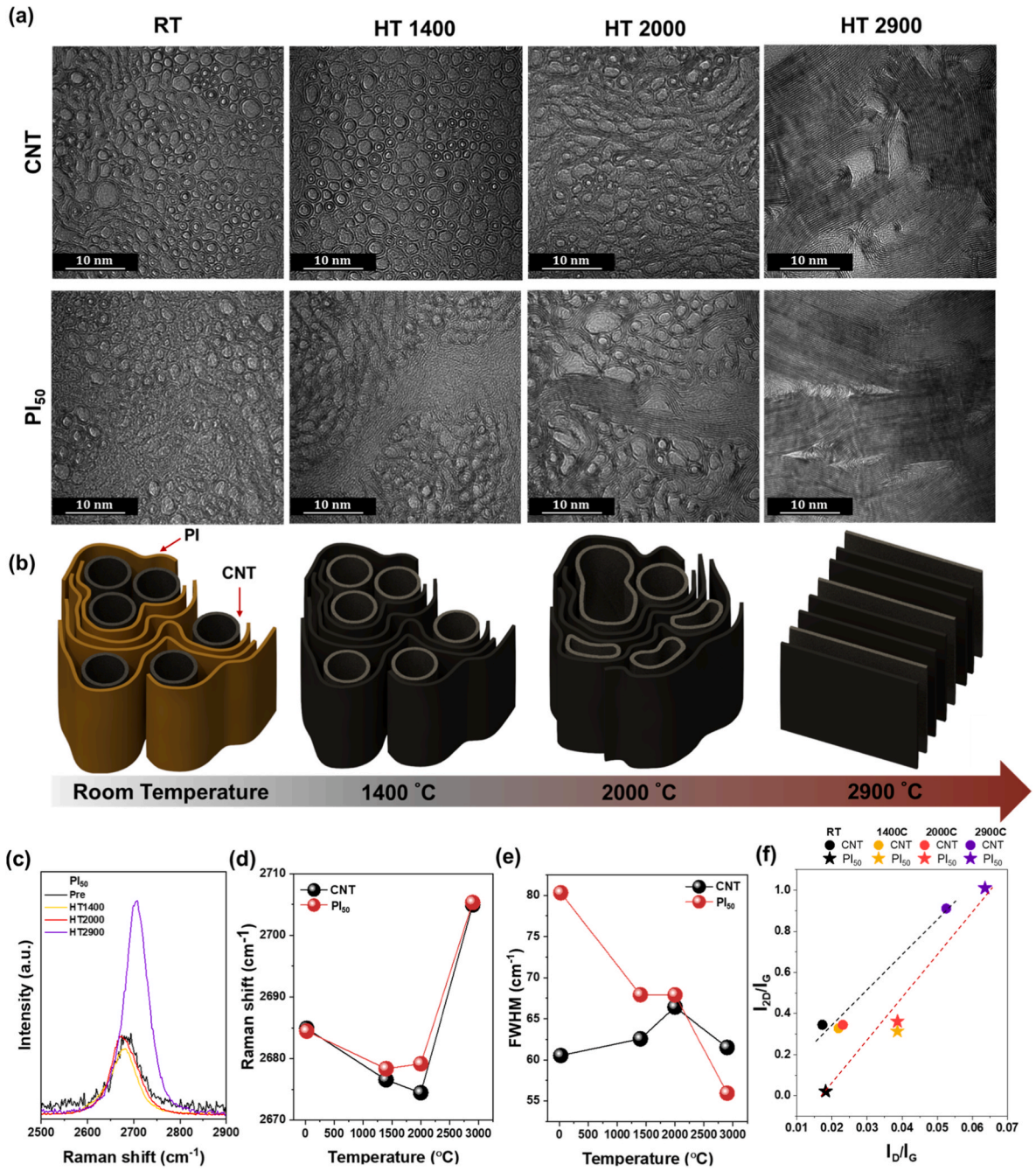

Fig. 4. Investigation of structural evolution as heat treatment temperature through (a) TEM and (b) its scheme. (c-f) Raman analysis of CNT and PI_{50} fiber. (c) 2D (G′)-band and its information with (d) FWHM, (e) Raman shift and (f) I_D/I_G vs. I_{2D}/I_G of the CNT and PI_{50} fiber.

3.5. Multimodal structural analysis of CNT vs PI_{50} fibers during high-temperature graphitization

Consistent with the Raman results, WAXS and SAXS analysis provided quantitative insights into the nanoscale ordering (Fig. 5). The correlation length of pristine CNT fibers peaked at 1400 °C, but rapidly declined with further heating-suggesting collapse and loss of long-range order (Fig. 5b). In contrast, PI_{50} fibers exhibited distinct temperature-dependent trends, reflecting the evolving role of the PI-derived scaffold. At room temperature, correlation length was dominated by the combined alignment of CNTs and PI chains, resulting in a longer correlation length compared to pristine CNT fibers. At 1400 °C, however, PI carbonization led to a temporary reduction in correlation length, whereas pristine CNT fibers benefited from CSA removal and axial alignment [49], producing their maximum correlation length. Specifically, CNT fibers that were only dried still retain trace amounts of residual CSA within the fiber interior. Upon heating to 1400 °C, evaporation of residual CSA induces capillary-driven densification, promoting closer packing and enhanced axial alignment of CNT bundles. This process increases inter-tube and inter-bundle structural coherence without altering the intrinsic graphitic structure of individual CNT walls [49]. With further heating to 2000 °C, the onset of PI graphitization enlarged the crystal domains, thereby increasing the correlation length. At 2900 °C, both CNT and PI were extensively graphitized; although tilting and stacking imperfections slightly reduced correlation length, the decrease was marginal compared to pristine CNTs. For the latter, structural collapse initiated at 2000 °C and became severe at 2900 °C, where the absence of a stabilizing scaffold prevented the preservation of

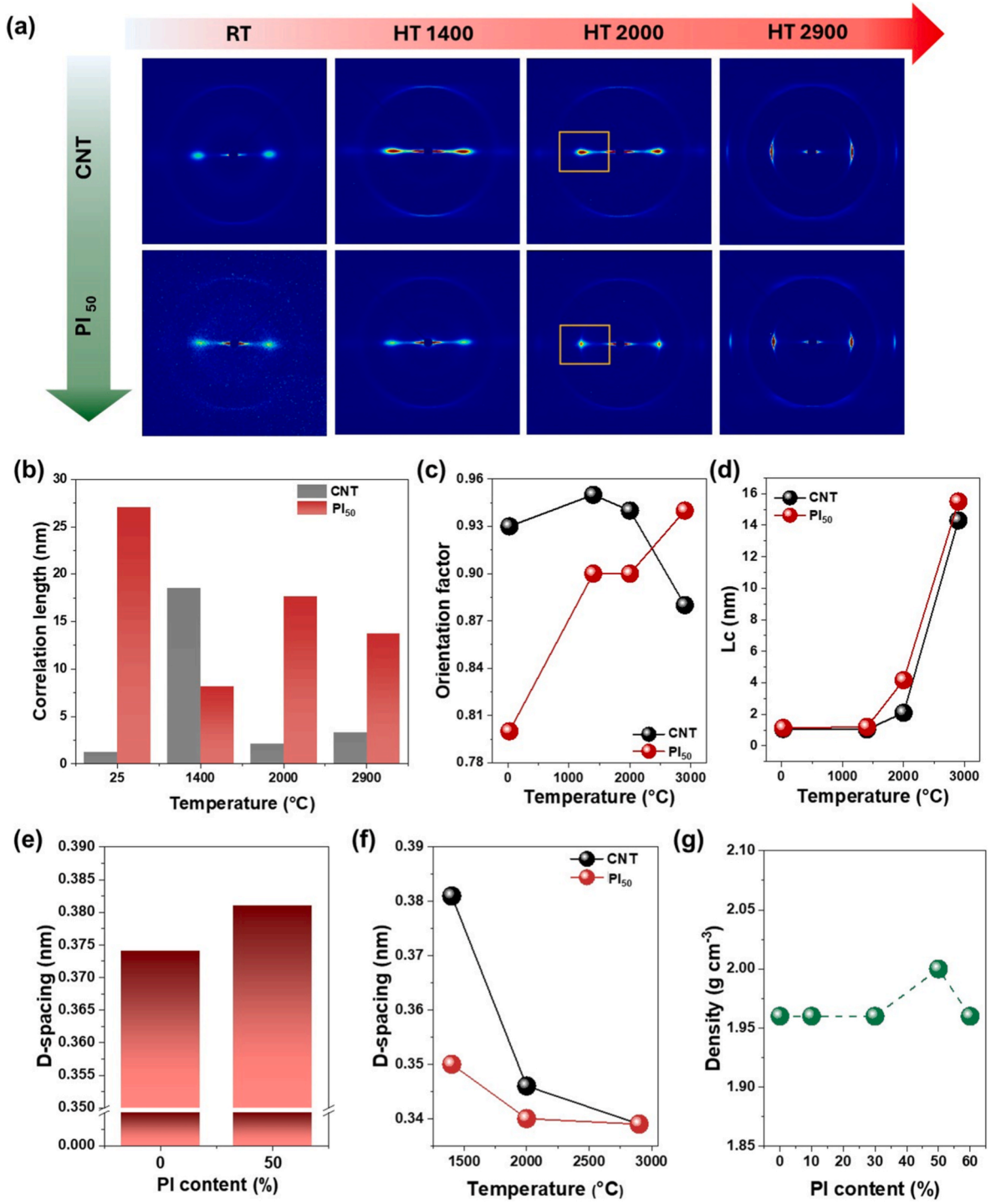

Fig. 5. Structure analysis of CNT and PI_{50} fibers according to the heat treatment temperature. (a) 2D WAXD pattern images, (b) correlation length through SAXS analysis of CNT and PI_{50} fibers. (c) Orientation factor, (d) out-of-plane of crystal size, D-spacing with (e) room temperature and (f) as heat treatment temperature. (g) Density of the fiber after graphitization at 2900 °C.

periodic ordering, yielding a markedly reduced correlation length.

WAXD analysis revealed corresponding changes in interlayer spacing and the (002) diffraction peak position (Fig. 5a, 5c-5g). For PI_{50} fibers, the orientation factor continuously increased with temperature, whereas pristine CNT fibers exhibited a decline above 1400 °C, indicating thermal misalignment and partial collapse (Fig. 5c and d). This trend highlights the scaffold-like role of carbonized PI in maintaining alignment, particularly around 2000 °C.

In parallel, the out-of-plane crystallite size (Lc) of both samples remained nearly unchanged at intermediate temperatures but increased sharply at 2900 °C, reflecting enhanced graphitic stacking. Furthermore, it led to faster structural evolution perpendicular to the fiber axis as shown in Fig. S10. Notably, the PI_{50} fibers exhibited a pronounced rise in Lc already at 2000 °C, suggesting that the carbonized PI not only stabilized the structure but also facilitated early-stage stacking, unlike the in-plane crystallite size (La), which showed a less distinct temperature dependence (Fig. S10). In the precursor state, the PI_{50} fibers exhibited a relatively larger interlayer spacing (d_{002}) of approximately 0.38 nm due

to the intercalation of PI chains between CNT bundles (Fig. 5e). Upon heat treatment at 1400 °C, PI began to be carbonized, leading to a substantial reduction in d-spacing to 0.35 nm and initiating early-stage graphitic packing (Fig. 5f). At 2000 °C, the scaffold-like role of the carbonized PI became more evident, as reflected in the equatorial WAXD patterns (Fig. 5a and Fig. S11). Compared to the pristine CNT fibers, the PI_{50} fibers exhibited a sharper (002) peak with higher diffraction angle, indicating enhanced stacking order and structural coherence facilitated by the PI. Also, in case of PI_{50} fibers, the orientation factor and out-of-plane crystallite size of the (002) plane increased with heat treatment temperature, while pristine CNT fibers lost their alignment above 1400 °C (Fig. 5e and f). In contrast, the in-plane crystallite size initially decreased due to PI carbonization but increased at 2900 °C, reflecting progressive structural reorganization (Fig. S10). This behavior reflects the ability of carbonized PI to promote CNT alignment and suppress structural collapse during intermediate stages of graphitization. As the temperature increased further to 2900 °C, the d-spacing of the PI_{50} fibers slightly decreased to 0.34 nm, approaching that of graphite. This trend is consistent with prior observations in PI-based carbon fibers or films, where heat treatment above 2000 °C progressively reduces interlayer spacing, reflecting enhanced graphitic stacking [50,51]. This result indicates that substantial structural densification had already occurred by 1400 °C. The carbonized PI acted as a robust scaffold, maintaining tight interlayer stacking and preventing structural relaxation during subsequent heat treatment. As a result, the PI_{50} fibers exhibited the highest fiber density of 2.0 g cm^{-3} among all the fibers (Fig. 5g), reflecting the formation of a tightly packed and well-ordered graphitic framework. In contrast, PI_{60} fibers showed a reduction in density, as the excess bulk-phase PI promoted void formation, which ultimately led to a less compact structure.

Collectively, multiscale structural analyses-Raman, SAXS, and WAXD-demonstrate that PI_{50} plays a critical role in stabilizing CNT frameworks during high-temperature treatment. The PI scaffold mitigates void misalignment, enhances axial ordering, and enables the formation of tightly packed graphitic domain. This structural coherence directly correlates with the superior thermal conductivity (534 W $m^{-1}K^{-1}$), electrical conductivity (0.64 MS m^{-1}), and tensile strength (3.26 GPa) achieved in PI_{50} fibers, underscoring the effectiveness of polymer-assisted structural engineering for high-performance carbon-based fibers. In comparison with commercial carbon fibers (Fig. 1e–f), PI-guided graphitization enables CNT composite fibers to achieve a density lower than pitch-based fibers while simultaneously delivering properties exceeding those of PAN-based carbon fibers. This dual advantage highlights the unique role of PI as a structural scaffold that overcomes the traditional trade-off between density and performance.

4. Conclusion

In this study, we demonstrated that incorporating polyimide (PI) into CNT fibers significantly improved their structural integrity and performance, particularly under high-temperature treatment up to 2900 °C. The PI component acted as a thermally stable scaffold that effectively suppressed CNT collapse and promoted the development of a highly ordered graphitic structure. Structural analyses using Raman spectroscopy, SAXS, and WAXD revealed that the CNT/PI composite fiber with content of 50% exhibited enhanced graphitic ordering, increased correlation length, and reduced void misalignment compared to pristine CNT fiber. As a result, the CNT/PI composite fiber with content of 50% achieved markedly higher tensile strength, electrical conductivity, and thermal conductivity. These findings highlight the critical role of PI in enabling the fabrication of robust, high-performance CNT-based fibers with stable architectures suitable for extreme processing conditions. They also point to molecular design of polymeric components as a promising pathway to further elevate the properties of CNT-based composite fibers.

CRediT authorship contribution statement

So Jeong Heo: Writing – original draft, Conceptualization. **Jiyeon Kim:** Validation, Formal analysis. **Jeong-Un Jin:** Validation, Formal analysis. **Changbeom Jeon:** Validation, Formal analysis. **Jungwon Kim:** Writing – review & editing. **Nam-Ho You:** Writing – original draft, Investigation, Conceptualization. **Han Gi Chae:** Writing – review & editing, Investigation, Conceptualization. **Seo Gyun Kim:** Writing – review & editing, Writing – original draft, Investigation, Conceptualization. **Bon-Cheol Ku:** Writing – review & editing, Writing – original draft, Investigation, Conceptualization.

Declaration of competing interest

The authors declare the following financial interests/personal relationships which may be considered as potential competing interests: Bon reports financial support was provided by Korea Institute of Science and Technology. Bon-Cheol Ku has patent #10-2725,246 issued to KIST. If there are other authors, they declare that they have no known competing financial interests or personal relationships that could have appeared to influence the work reported in this paper.

Acknowledgments

This work was supported by grants from the Institutional Program (2E33322) of the Korea Institute of Science and Technology (KIST) and the development project for high-performance carbon nanotube composite fiber manufacturing technology (RS-2023-00258521) Ministry of Trade, Industry & Energy (MOTIE) of Republic of Korea. The authors also acknowledge financial support from the Commercialization Promotion Agency for R&D Outcomes (RS-2023-00304729) by the Ministry of Science and ICT.

Appendix A. Supplementary data

Supplementary data to this article can be found online at https://doi.org/10.1016/j.carbon.2026.121428.

References

[1] M.F. Yu, O. Lourie, M.J. Dyer, K. Moloni, T.F. Kelly, R.S. Ruoff, Strength and breaking mechanism of multiwalled carbon nanotubes under tensile load, Science 287 (5453) (2000) 637–640.
[2] S.A. Meguid, G.J. Weng, Micromechanics and Nanomechanics of Composite Solids, Springer International Publishing : Imprint: Springer, Cham, 2018, p. 1, online resource (XIII, 519 pages 186 illustrations, 136 illustrations in color.
[3] J.W. Che, T. Çagin, W.I.I.I. Goddard, Thermal conductivity of carbon nanotubes, Nanotechnology 11 (2) (2000) 65–69.
[4] N. Behabtu, C.C. Young, D.E. Tsentalovich, O. Kleinerman, X. Wang, A.W.K. Ma, E. A. Bengio, R.F. ter Waarbeek, J.J. de Jong, R.E. Hoogerwerf, S.B. Fairchild, J. B. Ferguson, B. Maruyama, J. Kono, Y. Talmon, Y. Cohen, M.J. Otto, M. Pasquali, Strong, light, multifunctional fibers of carbon nanotubes with ultrahigh conductivity, Science 339 (6116) (2013) 182–186.
[5] Y.M. Song, S.X. Qiu, S.X. Feng, R. Zuo, Y.T. Zhang, K. Jia, X. Xia, M.M. Chen, K. M. Ji, C.Y. Wang, A review of carbon nanotubes in modern electrochemical energy storage, N. Carbon Mater. 39 (6) (2024).
[6] A.K.M.R. Reddy, A. Darwiche, M.V. Reddy, K. Zaghib, Review on advancements in carbon nanotubes: synthesis, purification, and multifaceted applications, Batteries-Basel 11 (2) (2025).
[7] S.G. Kim, S.J. Heo, S. Kim, J. Kim, S.O. Kim, D.J. Lee, S.H. Lee, J. Kim, N.H. You, M. Kim, H.C. Kim, H.G. Chae, B.C. Ku, Ultrahigh strength and modulus of polyimide-carbon nanotube based carbon and graphitic fibers with superior electrical and thermal conductivities for advanced composite applications, Compos Part B-Eng 247 (2022).
[8] S. Jo, A. Mikhalchan, S. Hong, S. Kim, S.G. Kim, S.M. Kim, D.Y. Kim, B.C. Ku, J. J. Vilatela, J.Y. Hwang, Highly conductive hybrid carbon nanotube fibers: strategies and future directions for replacing copper with next-generation conductors, Compos Part B-Eng 300 (2025).
[9] K.J. Hughes, K.A. Iyer, R.E. Bird, J. Ivanov, S. Banerjee, G. Georges, Q.A. Zhou, Review of carbon nanotube research and development: materials and emerging applications, ACS Appl. Nano Mater. 7 (16) (2024) 18695–18713.
[10] M. Rdest, D. Janas, Carbon nanotube films for energy applications, Energies 14 (7) (2021).

[11] S.E. Jung, S.G. Kim, T.H. Kim, J. Kim, M. Kim, D. Lee, D. Lee, B.C. Ku, S.H. Lee, Ultrathin, large-area, and multifunctional polarizer based on highly ordered carbon nanotubes produced by simple shear flow, Adv. Mater. Technol. (2023) 2301176.
[12] H. Song, H. Jeon, D. Im, N. Çakmakçi, K.Y. Shin, Y. Jeong, Free-standing carbon nanotube film for high efficiency monopole antenna, Carbon 187 (2022) 22–28.
[13] R. Paul, V. Etacheri, V.G. Pol, J.J. Hu, T.S. Fisher, Highly porous three-dimensional carbon nanotube foam as a freestanding anode for a lithium-ion battery, RSC Adv. 6 (83) (2016) 79734–79744.
[14] M.H. Lee, Y.H. Kong, J. Kim, Y.K. Lee, S.Y. Cho, Freely shapable and 3D porous carbon nanotube foam using rapid solvent evaporation method for flexible thermoelectric power generators, Adv. Energy Mater. 9 (29) (2019).
[15] Y.Z. Wu, X.W. Zhao, Y.Y. Shang, S.L. Chang, L.X. Dai, A.Y. Cao, Application-driven carbon nanotube functional materials, ACS Nano 15 (5) (2021) 7946–7974.
[16] D. Lee, S.J. Heo, S.G. Kim, B.C. Ku, A review of high-performance carbon nanotube-based carbon fibers, Funct. Compos. Struct. 5 (4) (2023).
[17] D. Lee, J. Kim, C.W. Kim, J.G. Kim, S.E. Jung, S.J. Heo, B.W. Im, N.D. Kim, S. G. Kim, Y. Piao, B.C. Ku, Nanocell-structured carbon nanotube composite fibers for ultrahigh energy and power density supercapacitors, Compos Part B-Eng 295 (2025).
[18] D.E. Tsentalovich, R.J. Headrick, F. Mirri, J.L. Hao, N. Behabtu, C.C. Young, M. Pasquali, Influence of carbon nanotube characteristics on macroscopic fiber properties, Acs Appl Mater Inter 9 (41) (2017) 36189–36198.
[19] D. Lee, S.G. Kim, J. Kim, N. Kim, K.H. Ryu, D.Y. Kim, N.D. Kim, J.Y. Hwang, Y. Piao, S. An, D.S. Lee, B.C. Ku, Highly conductive and mechanically strong metal-free carbon nanotube composite fibers with self-doped polyaniline, Carbon 213 (2023).
[20] S.G. Kim, S.J. Heo, J.G. Kim, S. Kim, D. Lee, M. Kim, N.D. Kim, D.Y. Kim, J. Y. Hwang, H.G. Chae, B.C. Ku, Ultrastrong hybrid fibers with tunable macromolecular interfaces of graphene oxide and carbon nanotube for multifunctional applications, Adv. Sci. 9 (29) (2022).
[21] M.Y. Zhang, H.Q. Niu, D.Z. Wu, Polyimide fibers with high strength and high modulus: preparation, structures, properties, and applications, Macromol. Rapid Commun. 39 (20) (2018).
[22] Y.Q. Wang, J.F. Zhou, J.R. Hou, X.Y. Chen, J. Sun, Q. Fang, High-performance polyimides with high and excellent dimensional stability at high temperature prepared via a cooperative action of hydrogen-bond interaction and cross-linking reaction, ACS Appl. Polym. Mater. 1 (8) (2019) 2099–2107.
[23] X.F. Xi Chen, Zhansheng Chen, Zaiteng Zhai, Hongkang Miu, Peng Tao, Multifunctional polyimide for packaging and thermal management of electronics: design, synthesis, molecular structure, and composite engineering, Nanomaterials 15 (15) (2025).
[24] M. Inagaki, N. Ohta, Y. Hishiyama, Aromatic polyimides as carbon precursors, Carbon 61 (2013) 1–21.
[25] H.W. Park, M. Lee, S.G. Kim, B.C. Ku, S.G. Jang, B.S. Kim, N.H. You, Crosslinked aromatic polyimides for high-performance heat-dissipation materials, J. Polym. Sci. 63 (15) (2025) 2997–3004.
[26] G.R. Zhang, S. Xue, F. Chen, Q. Fu, An efficient thermal interface material with anisotropy orientation and high through-plane thermal conductivity, Compos. Sci. Technol. 231 (2023).
[27] J.U. Jin, J.R. Hahn, N.H. You, Structural effect of polyimide precursors on highly thermally conductive graphite films, ACS Omega 7 (29) (2022) 25565–25572.
[28] R. Rath, P. Kumar, D. Rana, V. Mishra, A. Kumar, S. Mohanty, S.K. Nayak, Sulfonated PVDF nanocomposite membranes tailored with graphene oxide nanoparticles: improved proton conductivity and membrane selectivity thereof, J. Mater. Sci. 57 (5) (2022) 3565–3585.
[29] L.W. Taylor, O.S. Dewey, R.J. Headrick, N. Komatsu, N.M. Peraca, G. Wehmeyer, J. Kono, M. Pasquali, Improved properties, increased production, and the path to broad adoption of carbon nanotube fibers, Carbon 171 (2021) 689–694.
[30] T.C.M.A. Inc., M60J-HIGH MODULUS CARBON FIBER, Toray, 2018.
[31] G.Q. Xin, T.K. Yao, H.T. Sun, S.M. Scott, D.L. Shao, G.K. Wang, J. Lian, Highly thermally conductive and mechanically strong graphene fibers, Science 349 (6252) (2015) 1083–1087.
[32] B.W. Zhu, J. Liu, T.Y. Wang, M. Han, S. Valloppilly, S. Xu, X.W. Wang, Novel polyethylene fibers of very high thermal conductivity enabled by amorphous restructuring, ACS Omega 2 (7) (2017) 3931–3944.
[33] L. Zhong, L.J. Guo, J.C. Wang, Q. Song, H.J. Li, Y.Y. Li, Excellent heat transfer and mechanical properties of graphite material with rolled-up graphene layers, Carbon 208 (2023) 123–130.
[34] X.W. Yangsu Xie, Thermal conductivity of carbon-based nanomaterials: deep understanding of the structural effects, Green Carbon 1 (1) (2023) 47–57.
[35] A.F. Thünemann, W. Ruland, Microvoids in polyacrylonitrile fibers:: a small-angle X-ray scattering study, Macromolecules 33 (5) (2000) 1848–1852.
[36] B. Smarsly, M. Antonietti, T. Wolff, Evaluation of the small-angle x-ray scattering of carbons using parametrization methods, J. Chem. Phys. 116 (6) (2002) 2618–2627.
[37] G.S. Zhou, Y.Q. Liu, L.L. He, Q.G. Guo, H.Q. Ye, Microstructure difference between core and skin of T700 carbon fibers in heat-treated carbon/carbon composites, Carbon 49 (9) (2011) 2883–2892.
[38] D.H. Li, C.X. Lu, S.J. Du, G.P. Wu, Y. Yang, L.N. Wang, Structural features of various kinds of carbon fibers as determined by small-angle X-ray scattering, Appl Phys a-Mater 122 (11) (2016).
[39] Y.H. Katsuya Fukuyama, Chapter 3 – Small-Angle X-ray Scattering, Materials Science and Engineering of Carbon, Butterworth-Heinemann, Elsevier, 2016.
[40] A.H. Sexton, H. Suhonen, M.K. Huss-Hansen, H. Demchenko, J. Kjelstrup-Hansen, M. Schwartzkopf, M. Knaapila, Multi-scale correlation of impact-induced defects in carbon fiber composites using X-ray scattering and machine learning, Sci Rep-Uk 14 (1) (2024).
[41] S. Prevost, T. Lopian, M. Pleines, O. Diat, T. Zemb, Small-angle scattering and morphologies of ultra-flexible microemulsions, J. Appl. Crystallogr. 49 (2016) 2063–2072.
[42] D. Saurel, J. Segalini, M. Jauregui, A. Pendashteh, B. Daffos, P. Simon, M. Casas-Cabanas, A SAXS outlook on disordered carbonaceous materials for electrochemical energy storage, Energy Storage Mater. 21 (2019) 162–173.
[43] P. Debye, H.R. Anderson, H. Brumberger, Scattering by an inhomogeneous solid .2. the correlation function and its application, J. Appl. Phys. 28 (6) (1957) 679–683.
[44] P. Debye, A.M. Bueche, Scattering by an inhomogeneous solid, J. Appl. Phys. 20 (6) (1949) 518–525.
[45] M.S. Dresselhaus, G. Dresselhaus, R. Saito, Physics of carbon nanotubes, Carbon 33 (7) (1995) 883–891.
[46] M.S. Dresselhaus, G. Dresselhaus, A. Jorio, A.G. Souza, R. Saito, Raman spectroscopy on isolated single wall carbon nanotubes, Carbon 40 (12) (2002) 2043–2061.
[47] A.R. Sabina Botti, Tomas Rindzevicius, Michael Stenbæk Schmidt, Surface-enhanced raman spectroscopy characterization of pristine and functionalized carbon nanotubes and graphene, in: G.M.d. Nascimento (Ed.), Raman Spectroscopy, IntechOpen, London, 2018.
[48] T.C. Hirschmann, M.S. Dresselhaus, H. Muramatsu, M. Seifert, U. Wurstbauer, E. Parzinger, K. Nielsch, Y.A. Kim, P.T. Araujo, G′ band in double- and triple-walled carbon nanotubes: a Raman study, Phys. Rev. B 91 (7) (2015).
[49] S.J. Heo, J. Kim, G.M. Choi, D. Lee, B.W. Im, S.S. Kim, B.C. Ku, H.S. Lee, S.G. Kim, Microstructural evolution effects on the density of carbon nanotube fibers, Carbon 226 (2024).
[50] Y. Han, N.K. Mahanta, B.J. Wang, S.S. Wang, A.R. Abramson, M. Cakmak, Structural evolution in graphitization of nanofibers and mats from electrospun polyimide-mesophase pitch blends, Carbon 71 (2014) 303–318.
[51] H. Konno, K. Shiba, Y. Kaburagi, Y. Hishiyama, M. Inagaki, Carbonization and graphitization having of Kapton-type polyimide film having boron-bearing functional groups, Carbon 39 (11) (2001) 1731–1740.